A Novel Finite-Set Sliding-Mode Model-Free Predictive Current Control for PMSM Drives Without DC-Link Voltage Sensor

Xing Liu, *Graduate Student Member, IEEE*, Hui Yang, *Senior Member, IEEE*, Heyun Lin, *Senior Member, IEEE*, Feng Yu, *Member, IEEE*, and Yong Yang, *Senior Member, IEEE*

***Abstract*—Model predictive control (MPC) has attracted a lot of attention for power converters and motor drives in the last decade, owing to its merits such as explicit concept, excellent dynamic performance, and decent applicability in digital implementation. However, as a model-based method, classical MPC is heavily dependent on the system parameters of the plant under control. In this article, a novel finite-set sliding-mode model-free predictive current control (FS-SM-MFPCC) is proposed for permanent magnet synchronous machine (PMSM) drives, which combines the theory of sliding-mode control with MPC. The proposed strategy is thoroughly model-free, irrelevant for the dc-link voltage, and computationally light. The original version of the suggested strategy suffers from two flaws: 1) poor steady-state performance and 2) existent tracking errors, which are solved by using a simple correction algorithm and an extended control set coordinating with an improved cost function, respectively. The comparatively experimental results based on a 500-W PMSM drive are given to confirm the benefits of the proposed strategy.**

***Index Terms*—Model-free predictive current control, model predictive control (MPC), motor drives, permanent magnet synchronous machine (PMSM), power converters, sliding mode (SM).**

I. Introduction

MODEL PREDICTIVE CONTROL (MPC) has been actively developed for power converters in recent decades [1], thanks to the advancement of digital microprocessors. The concept of MPC is quite explicit, which accords with the discrete character of digital microprocessors. MPC takes several advantages such as good dynamic performance, feasibility for multiobjective control, and easy integration of nonlinear constraints [2], [3].

As a model-based technique, the most challenging issue encountered in MPC is the dependence on parameter accuracy [4]. However, parameter mismatches are inescapable in practical systems due to the changes in operating point and/or environment [5]. Obvious steady-state errors and weakened dynamic responsiveness will result if the parameter variations are not under consideration. Such deteriorations in control performance heavily impede the development of MPC in industrial applications.

Various solutions have been proposed in the literature [6], [7], [8], [9], [10], [11], [12], [13], [14], [15], [16], [17], [18], [19], [20] to avoid the problem of parameter dependence and enhance the robustness consequently. The most straightforward way is to identify or correct the involved parameters online by integrating online identification techniques. For example, an adaptive model predictive current control (MPCC) is proposed for a permanent magnet synchronous machine (PMSM) drive in [6], which integrates an adaptive observer. The *dq* inductances are identified online by the adaptive observer in a recursive manner. In [7], an inductance online identification method-based MPCC is proposed for a grid-connected voltage source inverter (VSI). The identification method corrects the inductance value in the control loop to its real one repeatedly. Nevertheless, the integration of online identification must aggravate the computational burden and, thus, complicate the implementation of MPC strategies [8].

To fundamentally tackle the issue of parameter dependence, model-free predictive control (MFPC) has attracted a lot of attention and has been a prominent branch within the family of MPC strategies for power electronics [9], [10]. As MFPC normally considers those variables that can be sampled directly, the currents are usually in control, instead of torque or flux, so model-free predictive current control (MFPCC) is a typical case at present. Existing MFPCC strategies can be loosely categorized into two groups. The first predicts the future current using the current differences associated with voltage vectors [11], [12]. The principle of this is very simple and straightforward. A severe challenge is ensuring the updating frequency of the current differences and, hence, the prediction

Manuscript received 25 May 2023; revised 14 August 2023; accepted 3 October 2023. Date of publication 6 October 2023; date of current version 6 December 2023. This work was supported in part by the National Natural Science Foundation of China under Grants 52037002 and 52077033, in part by the Key R&D Program of Jiangsu Province under Grant BE2021052, in part by the "Thousand Talents Plan" Project of Jiangxi Province under Grant jsxq2020102088, in part by the HighEnd Foreign Experts Recruitment Plan of China under Grant G2022141003L, and in part by the GF Key Laboratory of Science and Technology Foundation Project and National Key Laboratory of Electromagnetic Energy under Grant 6142217210201. Recommended for publication by Associate Editor J. Espinoza. *(Corresponding author: Hui Yang.)*

Xing Liu, Hui Yang, and Heyun Lin are with the School of Electrical Engineering, Southeast University, Nanjing 210096, China (e-mail: lyousying1996@163.com; huiyang@seu.edu.cn; hyling@seu.edu.cn).

Feng Yu is with the School of Electrical Engineering, Nantong University, Nantong 226019, China (e-mail: yufeng628@ntu.edu.cn).

Yong Yang is with the School of Rail Transportation, Soochow University, Suzhou 215131, China (e-mail: yangy1981@suda.edu.cn).

Color versions of one or more figures in this article are available at https://doi.org/10.1109/TPEL.2023.3322400.

Digital Object Identifier 10.1109/TPEL.2023.3322400

precision of future currents. To solve this problem, an improved current difference updating technique is proposed in [13], which allows the current differences of multiple voltage vectors to be updated simultaneously. However, another deficiency in terms of the sampling accuracy on currents is still unresolved [14].

Another kind of MFPCC is developed based on the ultralocal model (ULM) [15], which offers a general framework for describing most physical systems. The utilization of ULM in fact constructs the correlation between the inputs and outputs of systems. For example, in the context of PMSM drives, the voltages generated by the inverter and the stator currents can be deemed as the inputs and outputs, respectively. All parameter-related parts in the original mathematical model are described by a total disturbance term, which can be estimated by using observers, such as linear extended state observer (LESO) [16], sliding-mode observer (SMO) [17], and Luenberger observer (LO) [18]. After acquiring the total disturbance, the future currents can be easily predicted and controlled based on finite set (FS) or deadbeat (DB) MPC technique. Nonetheless, the design of the gain coefficient in the ULM actually relies on the value of inductance [19], although no parameters of the system are involved. At the same time, the compensations made for the inherent nonlinearities are crucial when implementing observers in digital systems [20].

Recently, the theory of sliding-mode (SM) control has been extended to MPC methods in [21], [22], and [23]. In [21], a quasi-SM predictive control is proposed, where a sliding surface predictive function is designed and integrated into a new cost function. In [22], the sliding surface predictive function is chosen in the same way as in [21], but a cost function satisfying the SM existence condition is proposed. These two works incorporate the SM control into MPC, but model-based predictions are still required. In [23], an approximatively model-free SM-based predictive control is proposed, where a simplified sliding surface is chosen and the cost function is designed in the same manner as for the work in [22]. This strategy is implemented in the *abc* frame for a bidirectional grid-connected VSI. The strategy is independent of the inductance value and the inner resistance value can be ignored due to its small value; therefore, "approximatively model-free" is utilized in the preceding description. However, this strategy is unsuitable for PMSM drives because the winding inductance values change with the position of the rotor. Furthermore, if the $\alpha\beta$ or *dq* frame is selected, the feature of inductance-independence will be disabled as well.

In this article, a novel finite-set SM MFPCC (FS-SM-MFPCC) is proposed for PMSM drives, which are fully model-free. The proposal takes two merits in addition to the model-free feature. On the one hand, the dc-link voltage information is irrelevant; therefore, the corresponding sensor can be removed. On the other hand, the computational burden of the proposed strategy is extremely low, since no predictions are needed and the cost function designed based on SM existence condition is very simple.

The main research contributions of this article can be summarized as follows.

1) For the first time, a substantially distinct FS-MFPCC incorporating the SM control theory is proposed. A very simple cost function is designed based on the SM existence condition, which is quite different from those utilized in the existing FS-MPC strategies.
2) Compared to the existing FS-MFPCC strategies, the proposed FS-SM-MFPCC not only dispenses with the information of dc-link voltage but significantly reduces the computational burden as well.
3) The proposed strategy is generic, although it is described and implemented based on a PMSM drive. The proposed strategy can be easily extended to most power electronics and motor drives, without sacrificing its simplicity and other distinct merits.

The rest of this article is organized as follows. First, the mathematical model of the PMSM drive, the traditional FS-MPCC, and the FS-MFPCC based on ULM are described in Section II. In Section III, the proposed FS-SM-MFPCC strategy is elaborated in terms of both advantages and disadvantages, and the associated improvements made for demerits are also included. The test results established on a 500-W PMSM drive are given in Section IV. Finally, Section V concludes this article.

II. Mathematical Model of PMSM Drive and Traditional FS-MPCC

A. Mathematical Model

The mathematical model of the PMSM drive in the *dq* frame can be expressed by a state-space equation, as

$$\begin{cases} \dot{\boldsymbol{x}} = \boldsymbol{A}\boldsymbol{x} + \boldsymbol{B}\boldsymbol{u} + \boldsymbol{C} \\ \boldsymbol{y} = \boldsymbol{E}\boldsymbol{x} \end{cases} \tag{1a}$$

with

$$\boldsymbol{x} = \boldsymbol{y} = \begin{bmatrix} i_d & i_q \end{bmatrix}^T,\ \boldsymbol{u} = \begin{bmatrix} u_d & u_q \end{bmatrix}^T \tag{1b}$$

$$\boldsymbol{A} = \begin{bmatrix} -\frac{R_s}{L_d} & \frac{\omega_r L_q}{L_d} \\ -\frac{\omega_r L_d}{L_q} & -\frac{R_s}{L_q} \end{bmatrix},\ \boldsymbol{B} = \begin{bmatrix} \frac{1}{L_d} & 0 \\ 0 & \frac{1}{L_q} \end{bmatrix} \tag{1c}$$

$$\boldsymbol{C} = \begin{bmatrix} 0 & -\frac{\omega_r \psi_f}{L_q} \end{bmatrix}^T,\ \boldsymbol{E} = \begin{bmatrix} 1 & 0 \\ 0 & 1 \end{bmatrix} \tag{1d}$$

where the cap "˙" means the differential operation; i_d and i_q are the *dq*-axis currents; u_d and u_q are the *dq*-axis voltages provided by the inverter; L_d and L_q are the *dq*-axis inductances; R_s is the stator resistance; ω_r and ψ_f are the electrical angular speed and the PM flux, respectively.

B. Traditional FS-MPCC

The principle of the traditional FS-MPCC method is exactly intuitive, which mainly consists of the following three steps:

1) using a prediction model to predict the future *dq*-axis currents for all voltage vectors provided by the inverter;
2) evaluating the voltage vectors using a cost function;
3) comparing the cost function values to find the optimal voltage vector.

The prediction model refers to the discretized version of the mathematical model, which can be deduced by the forward Euler

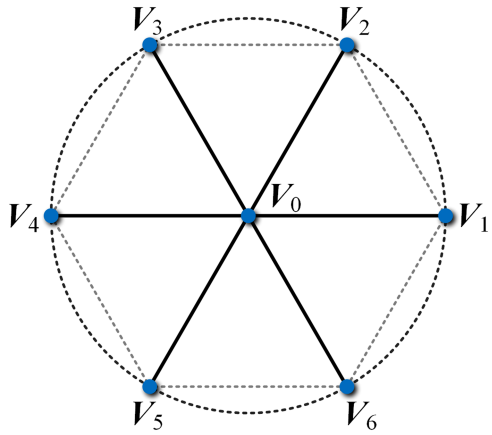

Fig. 1. Voltage vectors available in a two-level converter.

equation. Discretizing (1), it has

$$\boldsymbol{x}(k+1) = e^{T_s \boldsymbol{A}} \boldsymbol{x}(k) + T_s [\boldsymbol{B} u(k) + \boldsymbol{C}] \tag{2}$$

where "k" and "$k+1$" mean the current and the next sampling periods, respectively; T_s is the sampling period. This prediction model using system parameters implies the decoupling control of dq-axis currents, which is normally accomplished by introducing an additional feed-forward current controller into the traditional field-orientated control based on PI controllers [24].

On the other hand, the cost function defined in the two-norm of the current tracking errors is

$$g_{\text{MPCC}} = \|\boldsymbol{x}^* - \boldsymbol{x}(k+1)\|_2^2 \tag{3}$$

where $\boldsymbol{x}^* = [i_d{}^*,\ i_q{}^*]^T$ is the reference. The optimal input corresponds to the minimum value of the cost function, which can be selected by

$$\boldsymbol{V}_{opt} = \arg \min_{\boldsymbol{V}_i \in \boldsymbol{\nu}} g_{\text{MPCC}}(\boldsymbol{V}_i) \tag{4}$$

where $\boldsymbol{\nu} = \{\boldsymbol{V}_0, \boldsymbol{V}_1, \ldots, \boldsymbol{V}_6\}$ for a two-level converter, as shown in Fig. 1.

C. FS-MFPCC Based on ULM

In the FS-MFPCC approaches based on ULM, all parameter-related and unknown portions of the original mathematical model (1) are described by a total disturbance. Under this concept, the mathematical model can be rewritten using a simple form, as

$$\dot{\boldsymbol{x}} = \boldsymbol{D} + \boldsymbol{\alpha u} \tag{5}$$

where $\boldsymbol{D}$ represents the parameter-related and unknown parts of the system, $\boldsymbol{\alpha}$ is a two-dimensional coefficient matrix, which, in principle, is equal to the matrix $\boldsymbol{B}$ in (1).

The estimation of $\boldsymbol{D}$ is essential to this method, which can be realized by using state observers, such as LESO [16], SMO [17], and LO [18]. It is worth mentioning that the essence of these works is the same, although different observers are employed. From this fact, the control performance of the three methods should be very similar. Comparatively, LESO is simpler than SMO and LO in terms of digital implementation; therefore, in this work, the LESO-based FS-MFPCC (LESO-FS-MFPCC) is chosen as a representation of the ULM-based FS-MFPCC methods. In [16], the LESO is constructed to estimate $\boldsymbol{D}$, as

$$\begin{cases} \boldsymbol{e}_{rr} = \boldsymbol{z}_1 - \boldsymbol{i}_s \\ \dot{\boldsymbol{z}}_1 = \boldsymbol{z}_2 + \boldsymbol{\alpha u} - \beta_1 \boldsymbol{e}_{rr} \\ \dot{\boldsymbol{z}}_2 = -\beta_2 \boldsymbol{e}_{rr} \end{cases} \tag{6}$$

where $\boldsymbol{z}_1$ is the estimated value of $\boldsymbol{i}_s$, and $\boldsymbol{e}_{rr}$ is the error between the estimated and actual values of $\boldsymbol{i}_s$; $\boldsymbol{z}_2$ is the estimated value of $\boldsymbol{D}$; $\beta_1 = 2\omega_0$, $\beta_2 = {\omega_0}^2$ are coefficients, and ω_0 is in relation to the control frequency.

The prediction model obtained by discretizing (5) is

$$\boldsymbol{x}(k+1) = \boldsymbol{x}(k) + T_s [\boldsymbol{D} + \boldsymbol{\alpha u}]. \tag{7}$$

Besides, the cost function is the same as for the traditional FS-MPCC, as in (3).

III. Proposed FS-SM-MFPCC

This section introduces the SM control to the FS-MPCC in the beginning. Thereafter, the proposed FS-SM-MFPCC is explained in terms of both advantages and disadvantages, following which, the demerits are solved. Finally, a summary of the proposed strategy is presented and a qualitative comparison is made between the proposed and existing strategies.

A. SM-Based FS-MPCC

The SM-based FS-MPCC is introduced at first. It should be noted that the PMSM drive is under consideration, rather than the bidirectional grid-connected VSI investigated in [23]. Meanwhile, the dq frame rather than the abc frame is considered.

Choosing a sliding surface is the first step in SM control. In strategies considering current control, the stator current $\boldsymbol{i}_s = [i_d\ i_q]^T$ should track their reference $\boldsymbol{i}_s{}^* = [i_d{}^*\ i_q{}^*]^T$; therefore, the sliding surface could be defined as

$$\boldsymbol{\sigma}_s = \boldsymbol{i}_s - \boldsymbol{i}_s^* \tag{8}$$

where $\boldsymbol{\sigma}_s = [\sigma_d\ \sigma_q]^T$ and $\boldsymbol{\sigma}_s = [0\ 0]^T$ indicates the sliding surface. The existence of SM necessitates the satisfaction of the following conditions [25], as

$$\boldsymbol{\sigma}_s \dot{\boldsymbol{\sigma}}_s^T < 0. \tag{9}$$

The negative sign in this inequality implies the system evolvement toward the sliding surface, and the amplitude of $|\boldsymbol{\sigma}_s \dot{\boldsymbol{\sigma}}_s^T|$ determines the rate of such evolvement [25].

The references of dq-axis currents are considered to be constant during a sampling period; thus, it has

$$\dot{\boldsymbol{\sigma}}_s = \dot{\boldsymbol{x}}. \tag{10}$$

Then, (9) can be written by

$$\boldsymbol{\sigma}_s \dot{\boldsymbol{x}}^T < 0. \tag{11}$$

As the inductance values L_d and L_q are positive, (11) is equivalent to

$$\boldsymbol{\sigma}_s \boldsymbol{F}^T < 0 \tag{12a}$$

with

$$\boldsymbol{F} = \boldsymbol{A}'\boldsymbol{x} + \boldsymbol{u} + \boldsymbol{C}' = \begin{bmatrix} F_d & F_q \end{bmatrix}^T \tag{12b}$$

and

$$\boldsymbol{A}' = \begin{bmatrix} -R_s & \omega_r L_q \\ -\omega_r L_d & -R_s \end{bmatrix},\ C' = \begin{bmatrix} 0 \\ -\omega_r \psi_f \end{bmatrix}. \tag{12c}$$

The control goal is surely to find a voltage vector that can fulfill (11). To that goal, a cost function can be defined in a very simple form, as

$$g = \boldsymbol{\sigma}_s^T \boldsymbol{F} = \sigma_d F_d + \sigma_q F_q. \tag{13}$$

According to the SM existence condition (11), it can be concluded that only negative cost function values are beneficial for maintaining SM of operation. The optimum voltage vector can be easily found by comparing the cost function values associated with all possible voltage vectors, which belong to $\boldsymbol{\nu} = \{\boldsymbol{V}_0, \boldsymbol{V}_1, \ldots, \boldsymbol{V}_6\}$, as shown in Fig. 1. It should be noted that other nonlinear constraints can be included in (13) as well, such as switching frequency regulation [26] and capacitor voltage balancing in multilevel inverter systems [13].

B. Proposed FS-SM-MFPCC

In form, the cost function (13) differs significantly from a standard cost function designed as 1- or 2-norm. The two parts, $\sigma_d F_d$ and $\sigma_q F_q$, are practically linearly dependent on the dq-axis components of the input voltage $\boldsymbol{u}$, respectively. This feature is advantageous for a further simplification of the strategy, which is also the foundation of the proposed FS-SM-MFPCC.

Considering the linear dependence, F_d and F_q can be rewritten as

$$\begin{cases} F_d = u_d + f_d \\ F_q = u_q + f_q \end{cases} \tag{14}$$

where f_d and f_q are the parameter-dependent parts in $\boldsymbol{F}$, which are irrelevant to the input. In this way, the cost function can be further expressed as

$$\begin{aligned} g &= \sigma_d F_d + \sigma_q F_q = \sigma_d (u_d + f_d) + \sigma_q (u_q + f_q) \\ &= \underbrace{\sigma_d u_d + \sigma_q u_q}_{\text{parameter-independent}} + \underbrace{\sigma_d f_d + \sigma_q f_q}_{\text{parameter-dependent}}. \end{aligned} \tag{15}$$

This equation divides the cost function into parameter-independent and parameter-dependent portions. It can also be noted that the parameter-dependent portion is input-irrelevant; thus

$$\boldsymbol{V}_{\text{opt}} = \arg\min_{\boldsymbol{V}_i \in \boldsymbol{\nu}} g(\boldsymbol{V}_i) = \arg\min_{V_i \in \boldsymbol{\nu}} g_1(\boldsymbol{V}_i) \tag{16a}$$

with

$$g_1 = \sigma_d u_d + \sigma_q u_q. \tag{16b}$$

Furthermore, u_d and u_q can be calculated using

$$\begin{bmatrix} u_d \\ u_q \end{bmatrix} = \boldsymbol{T}_{abc/dq} \begin{bmatrix} u_{aN} \\ u_{bN} \\ u_{cN} \end{bmatrix} \tag{17}$$

with Park's transformation from the abc frame to the dq frame as

$$\boldsymbol{T}_{abc/dq} = \frac{2}{3} \begin{bmatrix} \cos\theta_e & \cos(\theta_e - 2\pi/3) & \cos(\theta_e + 2\pi/3) \\ -\sin\theta_e & -\sin(\theta_e - 2\pi/3) & -\sin(\theta_e + 2\pi/3) \end{bmatrix} \tag{18}$$

where u_{aN}, u_{bN}, and u_{cN} are the three-phase voltages in relation to the switching state of VSI and the dc-link voltage, expressed by

$$\begin{bmatrix} u_{aN} \\ u_{bN} \\ u_{cN} \end{bmatrix} = \frac{V_{dc}}{3} \begin{bmatrix} 2S_a - S_b - S_c \\ 2S_b - S_a - S_c \\ 2S_c - S_a - S_b \end{bmatrix}. \tag{19}$$

By defining

$$\begin{bmatrix} S_d \\ S_q \end{bmatrix} = \boldsymbol{T}_{abc/dq} \begin{bmatrix} 2S_a - S_b - S_c \\ 2S_b - S_a - S_c \\ 2S_c - S_a - S_b \end{bmatrix} \tag{20}$$

(16b) can be rewritten as

$$g_1 = \frac{V_{dc}}{3} (\sigma_d S_d + \sigma_q S_q). \tag{21}$$

On this basis, it is definitely true that

$$\boldsymbol{V}_{\text{opt}} = \arg\min_{\boldsymbol{V}_i \in \boldsymbol{\nu}} g_1(\boldsymbol{V}_i) = \arg\min_{\boldsymbol{V}_i \in \boldsymbol{\nu}} g_2(\boldsymbol{V}_i) \tag{22}$$

where

$$g_2 = \sigma_d S_d + \sigma_q S_q \tag{23}$$

The cost function g_2 is independent of parameters and dc-link voltage, and it is simpler than (13). This cost function introduces the parameter-independence feature, which allows the dc-link voltage sensor to be removed and further reduces the computational burden.

Despite the several advantages, it is foreseeable that the proposed FS-SM-MFPCC will suffer from the disadvantage of poor steady-state performance, since the selection of optimal voltage vector according to (23) aims to control the system evolvement toward the sliding surface as fast as possible (but not regulate the dq-axis current errors to zero). The simulation results of dq-axis currents using LESO-FS-MFPCC [16] and the proposed strategy are shown in Fig. 2. As seen, the q-axis current ripple of the proposed strategy almost doubles that of LESO-FS-MFPCC. Meanwhile, the steady-state tracking error of the q-axis current can be observed in the zoomed figure, although the current change at each sampling period can tend to the reference (i.e., the so-called SM of operation). The two issues are addressed in the following sections.

C. Suppression of Steady-State Tracking Errors

A simple and generic algorithm is proposed to suppress the dq-current tracking errors. The algorithm corrects the references of dq-axis currents. The error between the targeted and the sampled values is integrated to obtain the correction, which is then added to the targeted value. The algorithm can be described using

$$\begin{cases} i_{dc}^* = i_d^* + K \int (i_d^* - i_d) dt \\ i_{qc}^* = i_q^* + K \int (i_q^* - i_q) dt \end{cases} \tag{24}$$

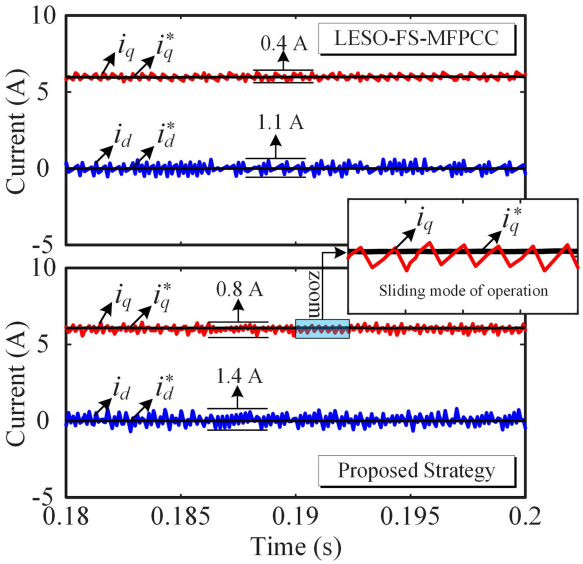

Fig. 2. Simulation results of LESO-FS-MFPCC and the proposed strategy.

where i_{dc}^* and i_{qc}^* are the corrected values of dq-axis references, respectively; K is the integral coefficient. The sliding surface should become

$$\boldsymbol{\sigma}_s = \boldsymbol{i}_s - \boldsymbol{i}_{sc}^* \tag{25}$$

with

$$\boldsymbol{i}_{sc}^* = \begin{bmatrix} i_{dc}^* & i_{qc}^* \end{bmatrix}^T. \tag{26}$$

D. Improvement of Steady-State Performance

The unsatisfactory steady-state performance is a remarkable disadvantage in the classic FS-MPCC, which is essentially caused by that the applied voltage vector leads to a large di/dt. The achievements in this field have put a lot of effort into improving the steady-state performance, by means of implicit modulation or extension of control set. The implicit modulation aims at selecting multiple vectors and calculating the corresponding duty cycles [27] while the extension of the control set is always based on constructing virtual voltage vectors [28]. Comparatively, the former is more attractive in terms of additional computational burden; however, the implementation always relies on the accurate prediction model. Therefore, this solution is incompatible with the proposed FS-SM-MFPCC.

Differently, the extension of the control set is more straightforward in theory and is applicable to the proposed strategy. The extended control set normally encompasses several sets of voltage vectors with different magnitudes; therefore, the control performance can be commensurate with a multilevel converter. When this solution is utilized in the traditional FS-MPCC, the additional computational burden is so severe owing to calculations of state prediction and cost function for the constructed virtual voltage vectors. Fortunately, in the proposed strategy, the calculations associated with voltage vectors are only conducted for the cost function (23), which is greatly simplified. Thus, the extension of the control set is utilized in this article for the improvement of steady-state performance.

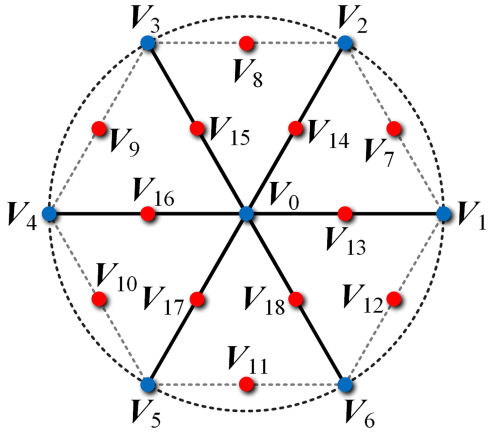

Fig. 3. Extended control set in this work.

TABLE I
VOLTAGE VECTORS IN THE EXTENDED CONTROL SET

Amplitude	Voltage Vector	α-axis component	β-axis component	Formulation
0	V_0	0	0	*N/A*
$2V_{dc}/3$	V_1	$2V_{dc}/3$	0	*N/A*
	V_2	$V_{dc}/3$	$\sqrt{3}V_{dc}/6$	*N/A*
	V_3	$-V_{dc}/3$	$\sqrt{3}V_{dc}/6$	*N/A*
	V_4	$-2V_{dc}/3$	0	*N/A*
	V_5	$-V_{dc}/3$	$-\sqrt{3}V_{dc}/6$	*N/A*
	V_6	$V_{dc}/3$	$-\sqrt{3}V_{dc}/6$	*N/A*
$\sqrt{3}V_{dc}/3$	V_7	$V_{dc}/2$	$\sqrt{3}V_{dc}/6$	$V_1/2 + V_2/2$
	V_8	0	$\sqrt{3}V_{dc}/6$	$V_2/2 + V_3/2$
	V_9	$-V_{dc}/2$	$\sqrt{3}V_{dc}/6$	$V_3/2 + V_4/2$
	V_{10}	$-V_{dc}/2$	$-\sqrt{3}V_{dc}/6$	$V_4/2 + V_5/2$
	V_{11}	0	$-\sqrt{3}V_{dc}/6$	$V_5/2 + V_6/2$
	V_{12}	$V_{dc}/2$	$-\sqrt{3}V_{dc}/6$	$V_6/2 + V_1/2$
$V_{dc}/3$	V_{13}	$V_{dc}/3$	0	$V_1/2 + V_0/2$
	V_{14}	$V_{dc}/6$	$\sqrt{3}V_{dc}/6$	$V_2/2 + V_0/2$
	V_{15}	$-V_{dc}/6$	$\sqrt{3}V_{dc}/6$	$V_3/2 + V_0/2$
	V_{16}	$-V_{dc}/3$	0	$V_4/2 + V_0/2$
	V_{17}	$-V_{dc}/6$	$-\sqrt{3}V_{dc}/6$	$V_5/2 + V_0/2$
	V_{18}	$V_{dc}/6$	$-\sqrt{3}V_{dc}/6$	$V_6/2 + V_0/2$

In this work, the extended control set $\boldsymbol{v}_e$ is composed of the original 7 voltage vectors ($\boldsymbol{V}_0$–$\boldsymbol{V}_6$) and 12 constructed virtual voltage vectors ($\boldsymbol{V}_7$–$\boldsymbol{V}_{18}$), as shown in Fig. 3, where the virtual voltage vectors are drawn with red dots. According to the amplitude, the 19 vectors can be categorized into 4 groups, as depicted in Table I. The original voltage vectors $\boldsymbol{V}_0$ and $\boldsymbol{V}_1$–$\boldsymbol{V}_6$ have magnitudes of 0 and $2V_{dc}/3$, respectively. Synthesizing all pairs of adjacent vectors with the same durations results in the virtual voltage vectors with a magnitude of $\sqrt{3}V_{dc}/3$ ($\boldsymbol{V}_7$–$\boldsymbol{V}_{12}$),

for instance, $\boldsymbol{V}_7 = \boldsymbol{V}_1/2 + \boldsymbol{V}_2/2$. Finally, $\boldsymbol{V}_{13}$–$\boldsymbol{V}_{18}$ are with a magnitude of $V_{dc}/3$, which are formulated by synthesizing $\boldsymbol{V}_0$ and $\boldsymbol{V}_1$–$\boldsymbol{V}_6$, such as $\boldsymbol{V}_{13} = \boldsymbol{V}_1/2 + \boldsymbol{V}_0/2$. The $\alpha\beta$-axis components of the 19 voltage vectors are also given in Table I, which can offer support for programming in experiments.

What should be noted is that the small voltage vectors (i.e., $\boldsymbol{V}_{13}$–$\boldsymbol{V}_{18}$) cannot be selected by minimizing (23). For instance, if the value of (23) corresponding to $\boldsymbol{V}_{13}$ can fulfill (11), i.e.,

$$g_2|_{\boldsymbol{u}=\boldsymbol{V}_{13}} < 0 \tag{27}$$

that corresponding to $\boldsymbol{V}_1$ fulfills the condition as well. Meanwhile, as the amplitude of $\boldsymbol{V}_1$ doubles that of $\boldsymbol{V}_{13}$, the following inequality always holds, as

$$g_2|_{\boldsymbol{u}=\boldsymbol{V}_1} < g_2|_{\boldsymbol{u}=\boldsymbol{V}_{13}} < 0. \tag{28}$$

This inequality implies that $\boldsymbol{V}_1$ is always superior to $\boldsymbol{V}_{13}$ under the evaluation criterion of (23). To address this problem, the cost function is further improved by introducing the amplitudes of S_d and S_q, as

$$g_3 = \sigma_d S_d + \sigma_q S_q + \lambda \left(|S_d| + |S_q|\right) \tag{29}$$

where λ is the weighting factor, which should be properly tuned for a better performance. By minimizing (29), the optimal voltage vector can be easily selected, as

$$\boldsymbol{V}_{opt} = \underset{\boldsymbol{V}_i \in \boldsymbol{\nu}_e}{\arg\min}\, g_3\left(\boldsymbol{V}_i\right). \tag{30}$$

E. Stability Analysis

Stability analysis is undoubtedly a crucial issue for control strategies. Till now, the publications giving the stability verification of FS-MPC methods for power electronics are still rare [29]. In this work, the stability of the proposed strategy is analyzed based on the Lyapunov function stability theory.

Lyapunov function stability theory states that the stability of the controlled system can be guaranteed if an energylike function [e.g., $V(x)$] exists and holds the following conditions except for the point $x = 0$: 1) $V(x)$ is positive definite and 2) the time derivative of $V(x)$ is negative definite. [30]

Considering the sliding surface chosen in (8), the constructed Lyapunov function can be expressed as

$$V\left(\boldsymbol{\sigma}_s\right) = \frac{1}{2}\left\|\boldsymbol{\sigma}_s\right\|_2^2. \tag{31}$$

There is no doubt that the condition i) is satisfied in the case of $\boldsymbol{\sigma}_s \neq [0\ 0]^T$. The satisfaction of condition ii) gives

$$\dot{V}\left(\boldsymbol{\sigma}_s\right) = \boldsymbol{\sigma}_s \dot{\boldsymbol{\sigma}}_s^T < 0. \tag{32}$$

This is exactly the existence condition of SM, which is mentioned in (9). The SM-based FS-MPCC is to find a voltage vector that can fulfill the existence condition of SM. In other words, the SM-based FS-MPCC naturally satisfies Lyapunov's stability criteria. Hence, the proposed FS-SM-MFPCC also satisfies Lyapunov's stability criteria, as the cos functions g, g_1, and g_2 are entirely equivalent.

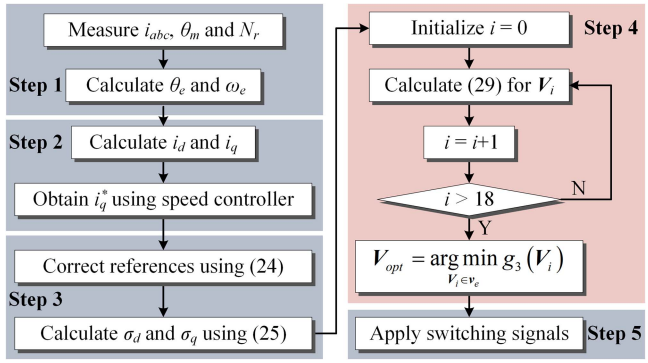

Fig. 4. Implementation flowchart of the proposed FS-SM-MPCC.

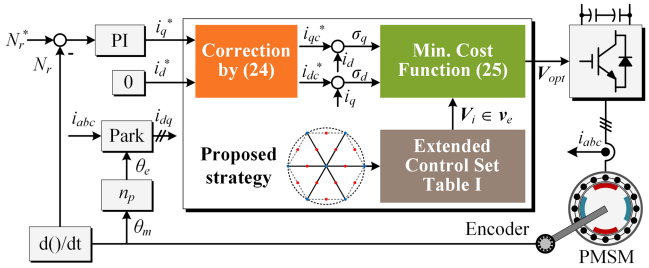

Fig. 5. Control diagram of the proposed FS-SM-MFPCC.

F. Summary and Digital Implementation of the Proposed FS-SM-MFPCC

The implementation flowchart and the control diagram of the proposed strategy are shown in Figs. 4 and 5, respectively. The following steps are required for digital implementation.

Step 1: Sample the stator currents (i_a, i_b, and i_c), acquire the rotor mechanical angle and speed (θ_m and N_r), and then calculate the electrical degree and the electrical angular speed (θ_e and ω_e).

Step 2: Calculate the dq-axis currents (i_d and i_q) using Park's transformation, and obtain the q-axis current reference (i_q^*) by means of the outer speed controller.

Step 3: Correct the dq-axis current references using (24), and calculate (25).

Step 4: Calculate the cost function (29) for all members in control set $\boldsymbol{\nu}_e$, and select the optimal voltage vector by comparing the obtained cost function values.

Step 5: Generate the corresponding switching signals to fire the inverter.

G. Qualitative Comparison Between Proposed Strategy and Existing Strategies

In this section, a qualitative comparison is made between the proposed and existing strategies, as shown in Table II. The basic FS-MPCC [2] and LESO-FS-MFPCC based on [16] have been explained in Section II. Moreover, the strategies developed in [21] and [23] are included, as their effort is also put into integrating the SM control with FS-MPC.

TABLE II
COMPARISON BETWEEN PROPOSED AND EXISTING STRATEGIES

Item	Basic FS-MPCC [2]	LESO-FS-MFPCC [16]	[21]	[23]	Proposed strategy
Modulator	No required	No required	No required	No required	No required
Multiobjective optim.	Yes	Yes	Yes	Yes	Yes
System parameters	Required	No required	Required	Partially required	No required
Tunable coefficients	No	$\boldsymbol{\alpha}$, ω_0	λ	No	k_i, λ
Cost function	$\left\|\boldsymbol{x}^*-\boldsymbol{x}(k+1)\right\|_2^2$	$\left\|\boldsymbol{x}^*-\boldsymbol{x}(k+1)\right\|_2^2$	[1] $\left\|\boldsymbol{s}^*-\boldsymbol{s}(k+1)\right\|_2^2$	[2] $\sum\sigma_k\left(v_{kn}-e_k-i_kR_k\right)$	$\sigma_dS_d+\sigma_qS_q+\lambda\left(\left\|S_d\right\|+\left\|S_q\right\|\right)$
DC-link voltage	Required	Required	Required	Required	No required

[1] $\boldsymbol{s}=\lambda\boldsymbol{x}+\dot{\boldsymbol{x}}$ is the sliding surface, which contains the weighting factor λ.
[2] $k=a$, b, or c, which denotes the grid phase, e_k is the grid voltage value of phase k, and $\sigma_k=i_k-i_k^*$ is the sliding surface.

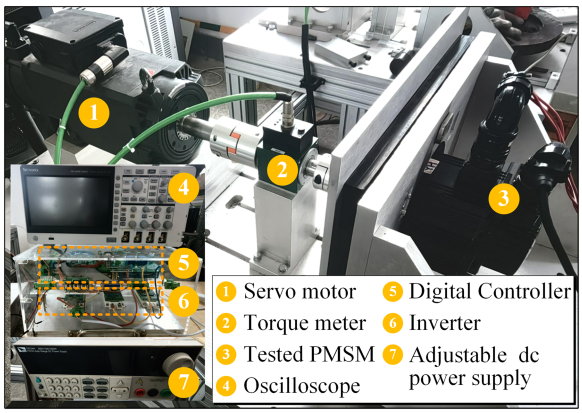

Fig. 6. Experimental test rig.

TABLE III
MAIN PARAMETERS OF THE TESTED PMSM

Symbol	Quantity	Value
V_{dc}	DC-link voltage	100 V
P_N	Rated power	500 W
n_N	Rated speed	800 r/min
n_p	Pole pairs	2
I_N	Rated current	7.5 A
R_s	Stator resistance	1.3 Ω
L_d	d-axis inductance	20 mH
L_q	q-axis inductance	39 mH
ψ_f	PM flux	0.261 Wb

TABLE IV
COEFFICIENTS OF FOUR STRATEGIES IN EXPERIMENTS

Strategy	Inner-loop	Outer-loop
Strategy #1	N/A	
Strategy #2	$\boldsymbol{\alpha}$ = [30 0; 0 30]; ω_0 = 7500	K_p = 0.25
Strategy #3	K = 5	K_i = 5
Strategy #4	K = 5; λ = 0.15	

The table shows two similarities between the offered methods. For one thing, no modulator is required in the presented methods, which is a characteristic of FS-MPC methods. For another thing, the presented methods are capable of multiobjective optimization, thanks to the use of the cost function. Thereafter, it is clear that both the LESO-FS-MFPCC and the proposed strategy do not require the system parameters while more tunable coefficients are included. Observing and comparing the cost functions, it is evident that the strategy in [21] is a variant of the basic FS-MPCC while the essence behind the proposed strategy and that in [23] is similar. Finally, a distinct advantage of the proposed strategy over others is that the information on dc-link voltage is not demanded. Overall, the proposed strategy inherits the good characteristics of FS-MPC and qualitatively holds merits of quite model-free characteristic and dc-link voltage independence.

IV. EXPERIMENTAL RESULTS

To verify the feasibility and effectiveness of the proposed FS-SM-MFPCC, an experimental test rig is constructed, as shown in Fig. 6. The PMSM under test is mechanically coupled with a servo machine that serves as the load, and a torque meter is placed between them. The main parameters of the PMSM are presented in Table III. The VSI consists of three FF300R12ME4 modules (Infineon), and an adjustable dc power supply is in the dc-link. Furthermore, the stator currents and the dc-link voltage are sampled by three current sensors HAS 50-S (LEM) and a voltage sensor LV25-P (LEM), respectively. The rotor position is acquired via a 2500-line incremental encoder, which is integrated into the PMSM casing. All sensed signals are fed into a digital signal processor TMS320F28335 (TI). The real-time programs are developed in C language on Code Composer Studio 7.4.0 software.

To experimentally corroborate the effectiveness of the proposed strategy, the traditional FS-MPCC, the LESO-FS-MPCC developed based on [16], and the two versions of the proposal are compared. For convenience, the traditional FS-MPCC and the LESO-FS-MFPCC are tagged with strategy #1 and strategy #2, respectively; meanwhile, the proposed strategy based on the control set $\boldsymbol{\nu}$ and the cost function (23) is termed strategy #3, and the proposed strategy based on the control set $\boldsymbol{\nu}_e$ and the cost function (29) is dubbed as strategy #4. It is worth noting that the dc-link voltage information is useless for strategies #3 and #4 but is mandatory in order for strategies #1 and #2 to be implemented.

The involved coefficients to be tuned in four strategies are summarized in Table IV, where K_p and K_i are the proportional and integral gains of the outer loop for speed control,

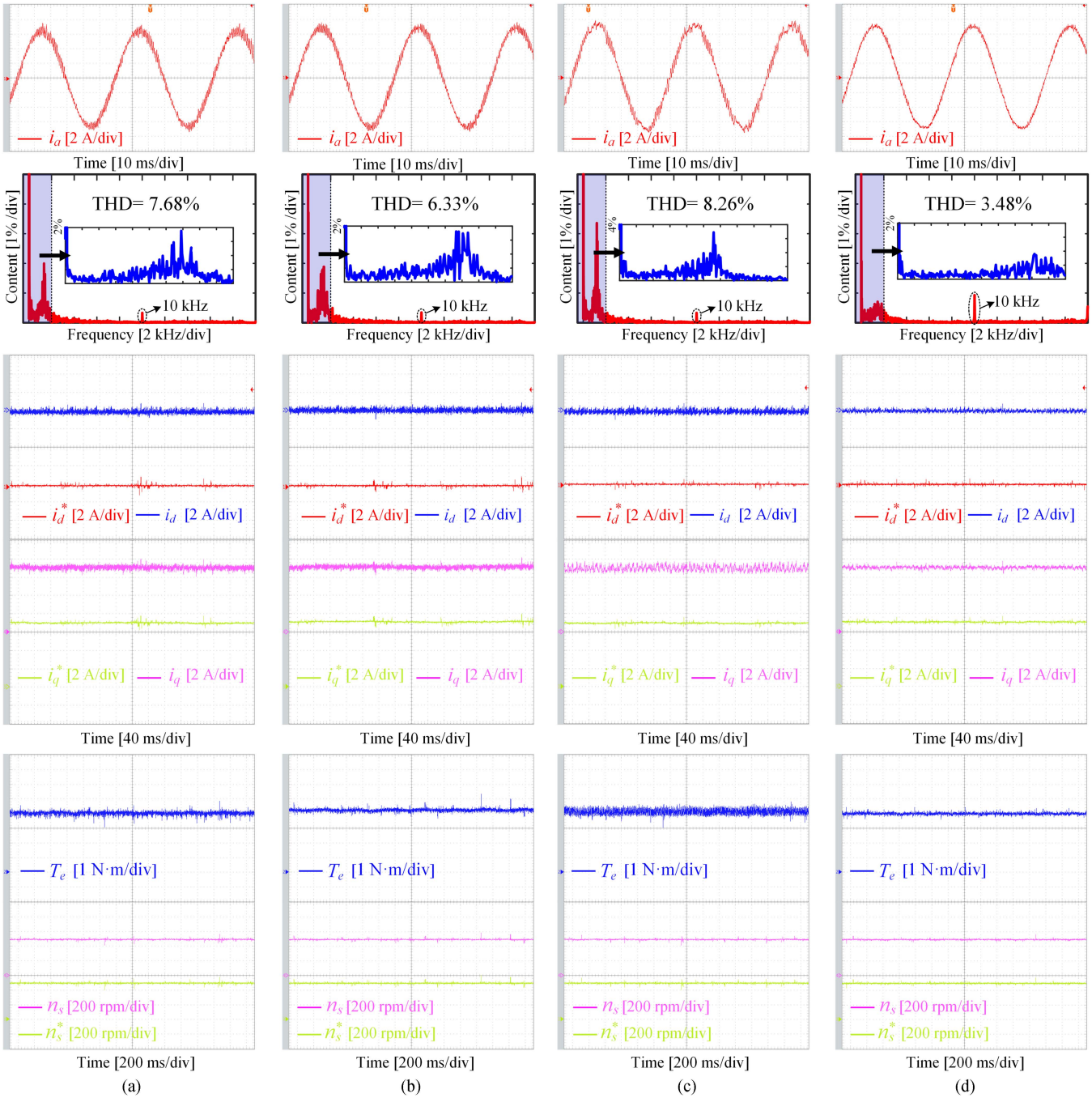

Fig. 7. Steady-state results of (a) strategy #1, (b) strategy #2, (c) strategy #3, and (d) strategy #4.

respectively. In order for a fair comparison, the PI gains of the outer-loop speed controller are designed to be the same for all evaluated strategies. The tuning of PI gains refers to the work in [31]. Regarding strategy #2, the matrix α is approximately set to [30 0; 030] considering the dq-axis inductances of the investigated PMSM, and ω_0 is set to 7500 in order to obtain a fast convergence of the LESO [32]. For Strategies #3 and #4, the coefficient K is set to 5 using a trial-and-error method while the weighting factor introduced in Strategy #4 is manually adjusted to 0.15. The sampling frequency is set as 10 kHz, as well as the control frequency, namely the sampling period $T_s = 100$ μs.

A. *Steady-State Performance*

At first, the steady-state performance is tested under the speed command of 500 revolutions per minute (r/min) with 4 N·m load. The results are shown in Fig. 7. It can be observed that all four strategies can yield sinusoidal stator current with a peak value of about 7 A; meanwhile, the dq-axis currents, the electromagnetic torque, and the speed can track the demands.

From the waveform of the stator current under strategy #3, a noticeable distortion can be seen while strategy #4 can generate a smoother curve thanks to the improvement discussed

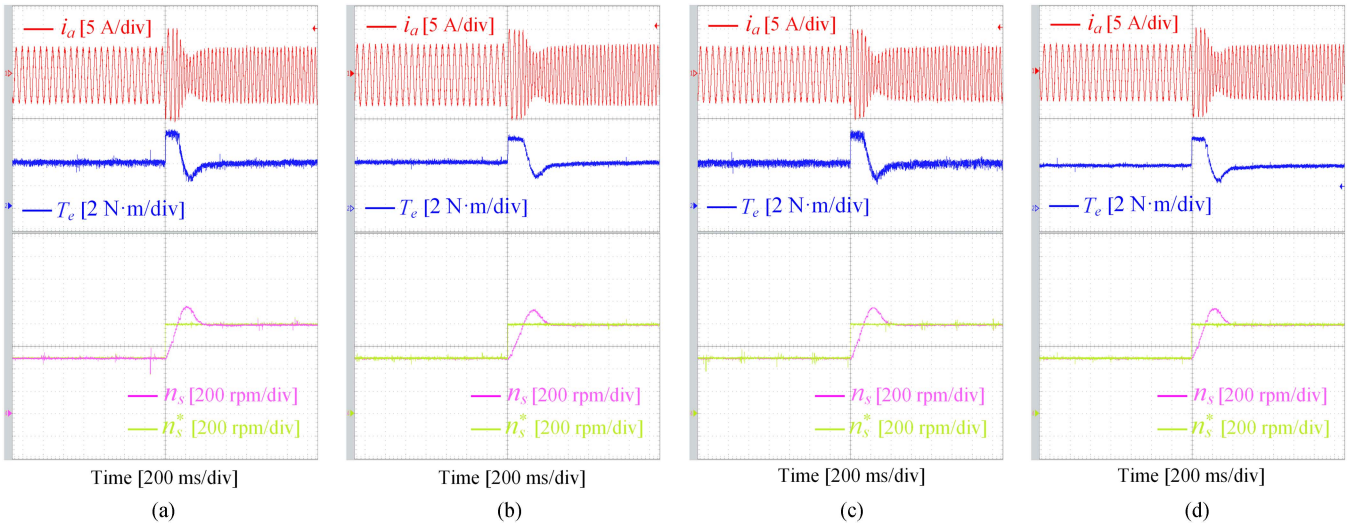

Fig. 8. Dynamic results of (a) strategy #1, (b) strategy #2, (c) strategy #3, and (d) strategy #4.

in Section III-D. According to the fast Fourier transform analysis results, the total harmonic distortion (THD) of i_a obtained using four strategies is 7.74%, 6.38%, 8.57%, and 3.61%, respectively. As observed, the harmonic content at 10 kHz is slight for strategies #1–#3, which is due to the dead-time effect of the inverter. In contrast, in strategy #4, more visible harmonics at the control frequency exist owing to the use of virtual vectors. At the same time, comparing the performance of four strategies in the low-frequency range, strategy #3 leads to more low-frequency harmonics and strategy #4 performs better.

In the results of *dq*-axis currents, it is easy to observe that the waveforms are irregular in strategies #1 and #2 while those curves in strategies #3 and #4 oscillate around the references, namely the SM of operation. This difference indicates the feature of SM control.

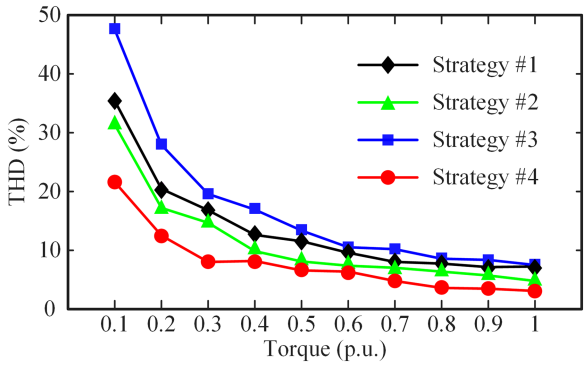

Fig. 9. THD results of stator current under different load conditions at 500 r/min.

B. Dynamic Performance

Then, the dynamic response of four strategies is compared, as illustrated in Fig. 8. The transient experiments follow an initial speed reference of 500 r/min with a step change to 800 r/min. The load is kept at 4 N·m. Strategies #1, #3, and #4 show a very similar dynamic response (response time of about 400 ms with an overshoot in the speed of 140 r/min) while the response time of strategy #2 (response time of about 440 ms with an overshoot in the speed of 120 r/min) is longer than others. As observed in Fig. 7(b), the electromagnetic torque in strategy #2 is lower than that in other strategies, although the stator current can reach the limit, which is set to 10 A in control programs. The cause might be that the LESO cannot accurately obtain the total disturbance in the step change condition, which results in the tracking errors of *dq*-axis currents. This test demonstrates the good dynamic performance of the proposed strategies.

C. Current THD Versus Load Torque

In addition, the THD of i_a under different load conditions is tested at 500 r/min, as concluded in Fig. 9, where 1 p.u. refers to 5 N·m. From the figure, it can be seen that the steady-state performances of strategies #1 and #2 are about equal in all conditions. The minor deficiency of strategy #1 can be explained by the unavoidable parameter mismatches in reality. Besides, it is verified that strategy #4 ranks first throughout the test while strategy #3 is always at the bottom. However, the performance of strategy #3 is very close to strategy #1 when the load torque is larger than half of the rating. This test shows the superiority of model-free strategies (including both the proposed strategies and the LESO-FS-MPCC) in practical implementation.

D. Switching Frequency Versus Speed

Thereafter, the average switching frequency of the inverter under changed speed conditions is tested in a manner where the load is set to 4 N·m. The results are presented in Fig. 10, where 1 p.u. corresponds to 800 r/min. It can be observed that in low-speed conditions, the average switching frequency of the inverter controlled by strategy #1 is slightly higher than that for strategy #2. When the speed is larger than 0.5 p.u., the switching frequency is nearly the same for strategies #1 and #2. In addition,

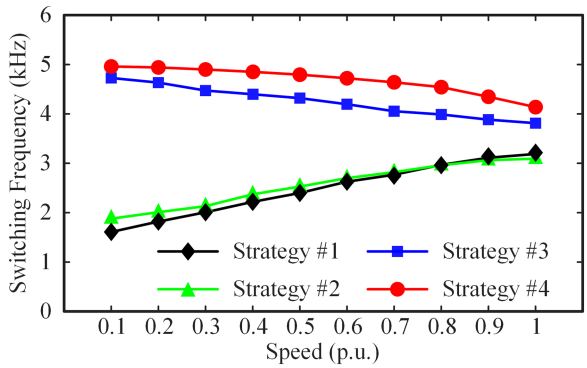

Fig. 10. Average switching frequencies of the inverter under changed speed conditions with the load of 4 N·m.

TABLE V
COMPUTATIONAL BURDEN COMPARISON

	Clock cycles	Execution time	Ratio
Strategy #1	4689	31.26 μs	1
Strategy #2	4258	28.39 μs	0.91
Strategy #3	2049	13.67 μs	0.44
Strategy #4	2589	17.26 μs	0.55

upward trends of change can be seen from the curves of strategies #1 and #2. Comparing the proposed two strategies, the average switching frequency generated by strategy #4 clearly exceeds that of strategy #3. This is as expected since each virtual vector used in strategy #4 is composed of two switching states.

Comparatively, in strategies #3 and #4, the switching frequency indicates downward trends of change, which are different from that in strategies #1 and #2. This distinction implies the different principles between the traditional predictive control strategies and the proposed ones. In addition, the comparison illustrates that the inverter may work at a higher switching frequency if the proposed strategies are activated.

At the same time, it must be noticed that the drawback of unfixed switching frequency exists in all strategies. There are many publications aiming at this issue as well, such as [33] and [34].

E. Computational Burden

Finally, the computational burdens of the four strategies are compared. The spent clock cycles are measured in the software by inserting breakpoints at the beginning and end of the interruptions triggered once per control period. The results are concluded in Table V. In addition to the spent clock cycles and the corresponding execution time, the ratios of the execution time of strategies #2–#4 with respect to that of strategy #1 are also presented. As seen, four strategies need about 31.26 μs, 28.39 μs, 13.67 μs, and 17.26 μs, respectively. The computational burden of strategy #2 is slightly less than that of strategy #1, which is attributed to the replacement of the traditional mathematical model by the simple ULM. Comparatively, strategy #3 shows a significant decrease in the computational burden, and the ratio is only 44%. Furthermore, as no model-based predictions are conducted and a very simple cost function is utilized, the computational burden of strategy #4 is merely 0.55 times of strategy #1, although 19 voltage vectors are included in the extended control set.

With the development of wide bandgap power semiconductors, such as SiC and GaN, the switching frequency of inverter can be up to tens of kilohertz in some applications [35], such as electric vehicles. The execution time of strategies #3 and #4 is less than 20 μs, which means that the inverter can operate at a frequency higher than 50 kHz. Such an improvement in terms of computational burden makes the proposed strategy more competitive and more attractive in the high-performance applications based on wide bandgap power semiconductors.

V. CONCLUSION

In this article, a novel FS-SM-MFPCC is proposed for PMSM drives, which integrates the theory of SM control with MPC. Compared with the existing methods, the proposed strategy has several merits, including completely model-free characteristics, dc-link voltage independence, and lower computational burden. The original version of the proposed strategy also suffers from problems of the existence of tracking errors and weak steady-state performance. A simple correction algorithm is proposed to suppress the tracking errors while the steady-state performance is enhanced by extending the control set and improving the cost function. The experimental results are given to verify the merits of the proposed strategies, and comparative studies are conducted among the basic FS-MPCC, the LESO-FS-MPCC, and two versions of the proposed strategy. It is shown that the improved version of the proposed strategy takes better steady-state performance, good dynamic response, and very low computational burden. The comparison in terms of switching frequency shows a difference in the trends of change of the switching frequency, which is because of the different principles of the traditional predictive control strategies and the proposed ones for selecting the optimal voltage vector.

REFERENCES

[1] J. Holtz, "Predictive finite-state control—When to use and when not," *IEEE Trans. Power Electron.*, vol. 37, no. 4, pp. 4225–4232, Apr. 2022.
[2] S. Vazquez, J. Rodriguez, and M. Rivera, "Model predictive control for power converters and drives: Advances and trends," *IEEE Trans. Ind. Electron.*, vol. 64, no. 2, pp. 935–947, Feb. 2017.
[3] K. K. Renjith, D. Sankar, and T. Hima, "A comprehensive review on finite control set model predictive control: Trends and prospects," in *Proc. 3rd Int. Conf. Intell. Comput. Instrum. Control Technol.*, 2022, pp. 206–210.
[4] J. Rodríguez, R. Heydari, and Z. Rafiee, "Model-free predictive current control of a voltage source inverter," *IEEE Access*, vol. 8, pp. 211104–211114, 2020.
[5] Y. Zhang, B. Xia, H. Yang, and J. Rodriguez, "Overview of model predictive control for induction motor drives," *Chin. J. Elect. Eng.*, vol. 2, no. 1, pp. 62–76, Jun. 2016.
[6] Z. Chen, J. Qiu, and M. Jin, "Adaptive finite-control-set model predictive current control for IPMSM drives with inductance variation," *IET Elect. Power Appl.*, vol. 11, no. 5, pp. 874–884, 2017.
[7] L. Guo, Z. Xu, and Y. Li, "An inductance online identification-based model predictive control method for grid-connected inverters with an improved phase-locked loop," *IEEE Trans. Transport. Electrific.*, vol. 8, no. 2, pp. 2695–2709, Jun. 2022.
[8] H. Yang, Y. Zhang, and W. Shen, "Predictive current control and field-weakening operation of SPMSM drives without motor parameters and DC voltage," *IEEE J. Emerg. Sel. Topics Power Electron.*, vol. 10, no. 5, pp. 5635–5646, Oct. 2022.

[9] J. Rodriguez et al., "Latest advances of model predictive control in electrical drives—Part I: Basic concepts and advanced strategies," *IEEE Trans. Power Electron.*, vol. 37, no. 4, pp. 3927–3942, Apr. 2022.
[10] J. Rodriguez et al., "Latest advances of model predictive control in electrical drives—Part II: Applications and benchmarking with classical control methods," *IEEE Trans. Power Electron.*, vol. 37, no. 5, pp. 5047–5061, May 2022.
[11] C. Lin, T. Liu, and J. Yu, "Model-free predictive current control for interior permanent-magnet synchronous motor drives based on current difference detection technique," *IEEE Trans. Ind. Electron.*, vol. 61, no. 2, pp. 667–681, Feb. 2014.
[12] C. Lin, J. Yu, and Y. Lai, "Improved model-free predictive current control for synchronous reluctance motor drives," *IEEE Trans. Ind. Electron.*, vol. 63, no. 6, pp. 3942–3953, Jun. 2016.
[13] F. Yu, C. Zhou, X. Liu, and C. Zhu, "Model-free predictive current control for three-level inverter-fed IPMSM with an improved current difference updating technique," *IEEE Trans. Energy Convers.*, vol. 36, no. 4, pp. 3334–3343, Dec. 2021.
[14] P. G. Carlet, F. Tinazzi, and S. Bolognani, "An effective model-free predictive current control for synchronous reluctance motor drives," *IEEE Trans. Ind. Appl.*, vol. 55, no. 4, pp. 3781–3790, Jul./Aug. 2019.
[15] M. Fliess and C. Join, "Model-free control," *Int. J. Control*, vol. 86, no. 12, pp. 2228–2252, 2013.
[16] Y. Zhang, J. Jin, and L. Huang, "Model-free predictive current control of PMSM drives based on extended state observer using ultralocal model," *IEEE Trans. Ind. Electron.*, vol. 68, no. 2, pp. 993–1003, Feb. 2021.
[17] Z. Sun, Y. Deng, J. Wang, T. Yang, Z. Wei, and H. Cao, "Finite control set model-free predictive current control of PMSM with two voltage vectors based on ultralocal model," *IEEE Trans. Power Electron.*, vol. 38, no. 1, pp. 776–788, Jan. 2023.
[18] N. Yang, S. Zhang, X. Li, and X. Li, "A new model-free deadbeat predictive current control for PMSM using parameter-free Luenberger disturbance observer," *IEEE J. Emerg. Sel. Topics Power Electron.*, vol. 11, no. 1, pp. 407–417, Feb. 2023.
[19] M. S. Mousavi, S. A. Davari, V. Nekoukar, C. Garcia, and J. Rodriguez, "Integral sliding mode observer-based ultralocal model for finite-set model predictive current control of induction motor," *IEEE J. Emerg. Sel. Topics Power Electron.*, vol. 10, no. 3, pp. 2912–2922, Jun. 2022.
[20] C. S. Lim, S. S. Lee, and E. Levi, "Continuous-control-set model predictive current control of asymmetrical six-phase drives considering system nonidealities," *IEEE Trans. Ind. Electron.*, vol. 70, no. 8, pp. 7615–7626, Aug. 2023.
[21] C. Zheng, Z. Gong, and X. Wu, "Finite-set quasi-sliding mode predictive control of *LC*-filtered voltage source inverters," *IEEE Trans. Ind. Electron.*, vol. 69, no. 12, pp. 11968–11978, Dec. 2022.
[22] O. Gulbudak, M. Gokdag, and H. Komurcugil, "Model predictive sliding surface control of voltage source inverter," in *Proc. IEEE Int. Conf. Power Electron., Smart Grid, Renewable Energy*, 2022, pp. 1–6.
[23] L. Estrada, N. Vazquez, and J. Vaquero, "Finite control set – model predictive control based on sliding mode for bidirectional power inverter," *IEEE Trans. Energy Convers.*, vol. 36, no. 4, pp. 2814–2824, Dec. 2021.
[24] J. Chen, J. Li, and R. Qu, "Analysis, modeling, and current trajectory control of magnetization state manipulation in variable-flux permanent magnet machines," *IEEE Trans. Ind. Electron.*, vol. 66, no. 7, pp. 5133–5143, Jul. 2019.
[25] R. DeCarlo, S. Zak, and G. Matthews, "Variable structure control of nonlinear multivariable systems: A tutorial," *Proc. IEEE*, vol. 76, no. 3, pp. 212–232, Mar. 1988.
[26] M. Aguirre, S. Kouro, and C. Rojas, "Enhanced switching frequency control in FCS-MPC for power converters," *IEEE Trans. Ind. Electron.*, vol. 68, no. 3, pp. 2470–2479, Mar. 2021.
[27] F. Yu, X. Liu, Z. Zhu, and J. Mao, "An improved finite-control-set model predictive flux control for asymmetrical six-phase PMSMs with a novel duty-cycle regulation strategy," *IEEE Trans. Energy Convers.*, vol. 36, no. 2, pp. 1289–1299, Jun. 2021.
[28] I. Hassine, M. Naouar, and N. Mrabet-Bellaaj, "Model predictive-sliding mode control for three-phase grid-connected converters," *IEEE Trans. Ind. Electron.*, vol. 64, no. 2, pp. 1341–1349, Feb. 2017.
[29] T. Li, X. Sun, and G. Lei, "Finite-control-set model predictive control of permanent magnet synchronous motor drive systems—An overview," *IEEE/CAA J. Automatica Sinica*, vol. 9, no. 12, pp. 2087–2105, Dec. 2022.
[30] H. Makhamreh, M. Trabelsi, O. Kükrer, and H. Abu-Rub, "A Lyapunov-based model predictive control design with reduced sensors for a PUC7 rectifier," *IEEE Trans. Ind. Electron.*, vol. 68, no. 2, pp. 1139–1147, Feb. 2021.
[31] L. Harnefors, K. Pietilainen, and L. Gertmar, "Torque-maximizing field-weakening control: Design, analysis, and parameter selection," *IEEE Trans. Ind. Electron.*, vol. 48, no. 1, pp. 161–168, Feb. 2001.
[32] Z. Gao, "Scaling and bandwidth-parameterization based controller tuning," in *Proc. Amer. Control Conf.*, 2003, pp. 4989–4996.
[33] S. Xu, Z. Sun, C. Yao, H. Zhang, W. Hua, and G. Ma, "Model predictive control with constant switching frequency for three-level T-type inverter-fed PMSM drives," *IEEE Trans. Ind. Electron.*, vol. 69, no. 9, pp. 8839–8850, Sep. 2022.
[34] Y. Yang et al., "An efficient model predictive control using virtual voltage vectors for three-phase three-level converters with constant switching frequency," *IEEE Trans. Ind. Electron.*, vol. 69, no. 4, pp. 3998–4009, Apr. 2022.
[35] S. Ghotgalkar et al., "High performance and EV power train system using C2000 MCU for functional safety," in *Proc. IEEE Int. Conf. Electron., Comput., Commun. Technol.*, 2022, pp. 1–5.

Xing Liu (Graduate Student Member, IEEE) was born in Huaian, China, in 1995. He received the B.Eng. and M.Sc. degrees in electrical engineering from Nantong University, Nantong, China, in 2018 and 2022, respectively. He is currently working toward the Ph.D. degree in electrical engineering with Southeast University, Nanjing, China.

His current research interests include the control strategies of power electronics and permanent magnet machines.

Hui Yang (Senior Member, IEEE) received the B.Eng. degree in electrical engineering from the Dalian University of Technology, Dalian, China, in 2011, and the Ph.D. degree in electrical engineering from Southeast University, Nanjing, China, in 2016.

From 2014 to 2015, he was supported by the China Scholarship Council through a one-year joint Ph.D. studentship with The University of Sheffield, Sheffield, U.K. Since 2016, he has been with Southeast University, where he has been an Associate Professor with the School of Electrical Engineering. From 2019 to 2020, he was a Postdoctoral Fellow with the School of Electrical Engineering, The Hong Kong Polytechnic University. He has authored or coauthored more than 80 IEEE transactions papers and was a peer reviewer of more than 10 IEEE journals. He is the holder of 40 patents. His research interests include novel permanent magnet machines and drives with particular reference to variable-flux machines for electric vehicles and renewable energy applications.

Dr. Yang is currently an Associate Editor for IEEE TRANSACTIONS ON INDUSTRIAL ELECTRONICS, an Associate Editor for IEEE TRANSACTIONS ON ENERGY CONVERSION, and an Editor of *World Electric Vehicle Journal*. He is also the TPC-Track Chair of IEMDC 2021 and the Organizing Committee Chair of CIEEC 2022. He is invited as a tutorial speaker for PESA 2020 and IEMDC 2021. He is the recipient of Best Paper Awards in ICEMS 2014, EVER 2015, ICEMS 2019, and EVS 34.

Heyun Lin (Senior Member, IEEE) received the B.S., M.S., and Ph.D. degrees in electrical engineering from the Nanjing University of Aeronautics and Astronautics, Nanjing, China, in 1985, 1989, and 1992, respectively.

From 1992 to 1994, he was a Postdoctoral Fellow with Southeast University, Nanjing. In 1994, he joined the School of Electrical Engineering, Southeast University, as an Associate Professor, and has been a Full Professor since 2000. He is the author of more than 150 technical papers and the holder of 30 patents. His main research interests include the design, analysis and control of permanent magnet motors, intelligent electrical apparatus, and electromagnetic field numerical analyses.

Dr. Lin is a Fellow of IET and also a member of the Electrical Motor and Apparatus Committee of Jiangsu Province, and a Senior Member of the China Society of Electrical Engineering and the China Electrotechnical Society.

Feng Yu (Member, IEEE) was born in Suzhou, China, in 1985. He received the B.Eng. degree in electrical engineering and automation from the School of Electrical Engineering, Sanjiang University, Nanjing, China, in 2008, the M.Sc. degree in electrical engineering from the School of Electrical and Information Engineering, Jiangsu University, Zhenjiang, China, in 2011, and the Ph.D. degree in electrical engineering from the Department of Electrical Engineering, Southeast University, Nanjing, in 2016.

Since 2016, he has been with Nantong University, Nantong, China, where he is currently a Full Professor with the School of Electrical Engineering. His current research interests include the control of multiphase machines and drives for applications ranging from automotive to renewable energy.

Yong Yang (Senior Member, IEEE) received the B.S. degree in automation from Xiangtan University, Xiangtan, China, in 2003, the M.S. degree in electrical engineering from Guizhou University, Guiyang, China, in 2006, and the Ph.D. degree in electrical engineering from Shanghai University, Shanghai, China, in 2010.

He is currently a Full Professor with the School of Rail Transportation, Soochow University. From December 2017 to December 2018, he was a Visiting Scholar with the Center for High Performance Power Electronics (CHPPE), The Ohio State University, Columbus, USA. He has coauthored more than 100 journal and conference papers. His current research interests include model predictive control in power electronic converters, distributed energy resource interfacing, and high-performance motor drive control.